Cement and Concrete Research 38 (2008) 1148–1153

Contents lists available at ScienceDirect

Cement and Concrete Research

journal homepage: http://ees.elsevier.com/CEMCON/default.asp

Determination of the elastic constants of portlandite by Brillouin spectroscopy

S. Speziale [a,*], H.J. Reichmann [a], F.R. Schilling [a], H.R. Wenk [b], P.J.M. Monteiro [c]

[a] Deutsches GeoForschungsZentrum, Telegrafenberg, 14473 Potsdam, Germany
[b] Department of Earth and Planetary Science, University of California, Berkeley, CA 94720-4767, U.S.A.
[c] Department of Civil and Environmental Engineering, University of California, Berkeley, CA 94720-1710, U.S.A.

ARTICLE INFO

Article history:
Received 17 October 2007
Accepted 28 May 2008

Keywords:
$Ca(OH)_2$
Elastic moduli
Cement

ABSTRACT

The single crystal elastic constants C_{ij} and the shear and adiabatic bulk modulus of a natural portlandite ($Ca(OH)_2$) crystal were determined by Brillouin spectroscopy at ambient conditions. The elastic constants, expressed in GPa, are: C_{11}=102.0(±2.0), C_{12}=32.1(±1.0), C_{13}=8.4(±0.4), C_{14}=4.5(±0.2), C_{33}=33.6(±0.7), C_{44}=12.0(±0.3), C_{66}=(C_{11}–C_{12})/2=35.0(±1.1), where the numbers in parentheses are 1σ standard deviations. The Reuss bounds of the adiabatic bulk and shear moduli are K_{0S}=26.0(±0.3) GPa and G_0=17.5(±0.4) GPa, respectively, while the Voigt bounds of these moduli are K_{0S}=37.3(±0.4) GPa and G_0=24.4(±0.3) GPa. The Reuss and Voigt bounds for the aggregate Young's modulus are 42.8(±1.0) GPa and 60.0(±0.8) GPa respectively, while the aggregate Poisson's ratio is equal to 0.23(±0.01). Portlandite exhibits both large compressional elastic anisotropy with C_{11}/C_{33}=3.03 (±0.09) equivalent to that of the isostructural hydroxide brucite ($Mg(OH)_2$), and large shear anisotropy with C_{66}/C_{44}=2.92(±0.12) which is 11% larger than brucite. The comparison between the bulk modulus of portlandite and that of lime (CaO) confirms a systematic linear relationship between the bulk moduli of brucite-type simple hydroxides and the corresponding NaCl-type oxides.

1. Introduction

Portlandite, $Ca(OH)_2$, is one of the most simple hydrous minerals. It has a trigonal symmetry with the space group *P*31 (e.g. [1]) and is isostructural to brucite. The structure of portlandite is based on layers of distorted edge sharing CaO_6 octahedra stacked along the *c*-axis. The layers are separated by H atoms bonded with oxygens of the octahedral layer. Each oxygen atom is protonated with hydrogens dynamically disordered around the 3-fold axis with a maximum of probability density aligned along the *c*-axis at ambient conditions [2,3].

Portlandite is of great interest in cement and concrete research and for the cement industry because it is a primary solid phase in hydrated portland cement, representing as much as 20–25% of the cement paste's volume [4,5]. Its thermal and mechanical behavior affects the properties of cement and concrete, therefore it is important to determine the elastic properties of portlandite. The knowledge of the elastic stiffness tensor of portlandite will allow the determination of the local stress field at the interfacial transition zone between the aggregate and the cement paste where portlandite crystals tend to precipitate with a preferred orientation near the aggregate [6,7]. Furthermore portlandite has been used as an internal strain gauge in neutron diffraction experiment of frozen cement paste [8,9]. The conversion of the measured strains to stresses requires accurate values of the elastic coefficients of portlandite. Finally, due to its simple composition and structure, portlandite is an ideal model to evaluate the effect of OH on the elastic properties in more complex hydrous minerals, with implications for the understanding of the mechanisms of water recycling in the Earth's interior.

Single-crystal elasticity of portlandite has been the subject of both computational and experimental studies. Laugesen [10] calculated the elastic coefficients C_{ij} of $Ca(OH)_2$ by means of density functional method. Holuj et al. [11] determined the C_{ij} utilizing Brillouin interferometry. However, the results of these two reports differ significantly in some constants, as in the case of C_{13} whose experimental value is 3 times larger than the values obtained from the density functional calculations. In this paper we report the full set of elastic constants C_{ij} at ambient conditions by means of Brillouin spectroscopy, and we resolve the existing discrepancy between experimental and first principles results.

2. Sample

Single-crystals of portlandite were picked from a natural specimen, sampled in the Wessel Mine, in the Kalahari Manganese Field (South Africa). The specimen is a bulk aggregate consisting of about 10 platy crystals with almost constant orientation and maximum dimension up to 2 cm. The density of our sample material ρ=2.242 (±0.003)×10^3 (kg/m^3) has been determined at the Deutsches GeoForschungs-Zentrum (GFZ) by powder X-ray diffraction using a STOE diffracto-meter equipped with a position sensitive detector. The incident radiation was monochromatic Cu $K_{\alpha 1}$. The unit cell parameters were

* Corresponding author.
E-mail address: speziale@gfz-potsdam.de (S. Speziale).

0008-8846/$ – see front matter © 2008 Elsevier Ltd. All rights reserved.
doi:10.1016/j.cemconres.2008.05.006

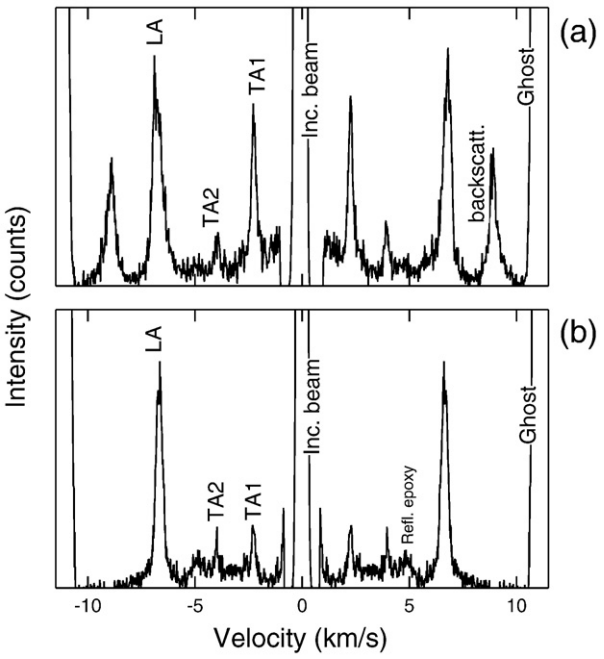

Fig. 1. Brillouin spectra of portlandite. (a) Basal plane (0.1 0 1). (b) Axial plane (0.1 0.6 – 0.1). LA: sample quasi-longitudinal acoustic mode; TA1, TA2: slow and fast sample quasi-transverse acoustic modes; backscatter.: backscattered sample longitudinal acoustic mode; Refl. epoxy: longitudinal acoustic mode from the epoxy glue surrounding the sample; Ghost: elastically scattered light.

determined based on the reflections in the 2θ range between 5 and 90°. The measured unit cell parameters are a_0=3.5927(±0.0009) Å and c_0=4.908(±0.005) Å, the unit cell volume is 54.87(±0.06) Å^3, in good agreement with the available data in the literature [1,12,13].

3. Brillouin scattering

Few crystals were cut into platelets both parallel to the perfect basal cleavage and roughly perpendicular to the basal cleavage. The platelets were ground to a thickness of about 300 μm and polished to 1 μm grit-size. The orientations of the platelets were refined by analyzing the Brillouin scattering results and are (0.1 0 1) and (1 0.6 – 0.1). For simplicity the two platelets will hereafter be referred to as "basal" and "axial" respectively. The two platelets were glued to glass capillaries, mounted on a goniometer head and positioned in the Eulerian cradle of the Brillouin system at GFZ Potsdam.

Brillouin scattering measurements were performed in forward scattering geometry with an external scattering angle (defined as the angle between incident and scattered beam outside the sample platelet) of 90°. The incident laser beam (λ=532.15 nm) was focused on the sample in the Eulerian cradle. The inelastically scattered light was then imaged on the entrance pinhole of a Sandercock six-pass tandem Fabry–Perot interferometer [14], which is able to resolve the Brillouin peaks from the central Rayleigh line; a photomultiplier tube was used as a detector. Brillouin frequency shifts were determined by peak-fitting the Brillouin spectral features. Sound velocities can be determined from Brillouin frequency shift as:

$$V_{P,S} = \Delta\omega_{P,S}\lambda/(2\sin(\theta/2)), \quad (1)$$

where $V_{P,S}$ is the compression or shear sound wave velocity, $\Delta\omega_{P,S}$ is the frequency shift of the Brillouin peaks associated to the compression or shear acoustic modes, λ is the laser wavelength, and θ is the external scattering angle as defined above. Due to the platelet geometry of the samples, the calculation of the sound wave velocities is independent from the refractive index n [15]. In the analysis of the Brillouin scattering data we have treated portlandite as an optically isotropic medium. Even though this is not strictly true (the maximum birefringence is 0.027, [11]) it has been demonstrated that this approximation is perfectly adequate to the available experimental resolution, even for strongly anisotropic materials like calcite (maximum birefringence ~0.15) [16].

Brillouin scattering was measured in 36 directions both in the basal and the axial sample platelets. The elastic constants have been retrieved from the measured velocities by nonlinear least-square inversion of the Christoffel's equation (e.g. [17,18])

$$(C_{iklm}l_k l_m - \rho m^2\delta_{il})u_l = 0, \quad (2)$$

where C_{iklm} are the elastic constants in tensor notation, l_k and l_m are the direction cosines of the phonon, u_l is the displacement vector, ρ is the density, ν is phonon's velocity, and δ_{il} is the Kronecker delta.

4. Results

In all the spectra, we have observed three different Brillouin peaks corresponding to the three polarizations (two quasi-shear and one quasi-longitudinal) of the acoustic wave propagating in the probed direction, that is, more than 200 different velocities were used in the inversion of the Christoffel's equation to constrain the full elastic tensor of portlandite. Examples of Brillouin spectra from both basal and axial platelet are shown in Fig. 1. The spatial dispersion of compressional and shear velocity are plotted in Fig. 2.

The values, expressed in GPa, for the single crystal elastic constants at ambient conditions are: C_{11}=102.0(±2.0), C_{12}=32.1(±1.0), C_{13}=8.4

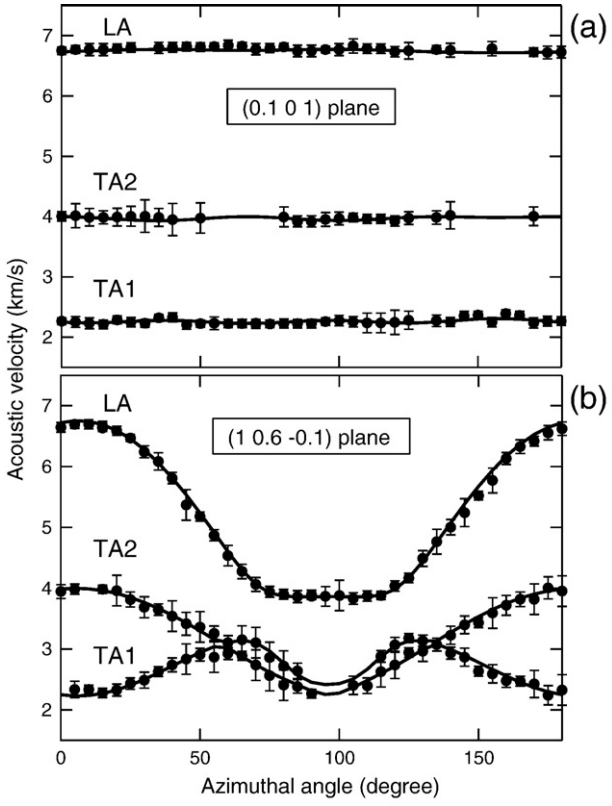

Fig. 2. Spatial dispersion of acoustic velocity in portlandite. (a) Basal plane (0.1 0 1). (b) Axial plane (0.1 0.6 – 0.1). LA: quasi-longitudinal velocity; TA1, TA2: slow and quasi-transverse velocity. Circles: measured velocities. Lines velocities calculated according to the elastic constants determined in this study.

Table 1
Adiabatic single crystal elastic constants of portlandite and—as comparison—of brucite; all units in GPa

	This work (Brillouin)	Laugesen [10] (DFT*)	Holuj et al. [11] (Brillouin)	$Mg(OH)_2$, brucite Jiang et al. [24]
C_{11}	102.0(±2.0)	99.39	99.28(±1.5)	154.0(±1.4)
C_{12}	32.0(±1.0)	30.78	36.21(±2.0)	42.1(±1.7)
C_{13}	8.4(±0.4)	7.36	29.65(±15.0)	7.8(±2.5)
C_{14}	4.5(±0.2)	≈0 (assumed)	≈0 (assumed)	1.3(±1.0)
C_{33}	33.6(±0.7)	36.29	32.60(±2.0)	49.7(±0.7)
C_{44}	12.0(±0.3)	7.88	9.846(±2.0)	21.3(±0.4)
C_{66}**	35.0±(1.1)	34.31	31.55(±1.5)	55.9(±1.7)

*Density functional theory calculations.
**$C_{66}=(C_{11}-C_{12})/2$.

(±0.4), C_{14}=4.5(±0.2), C_{33}=33.6(±0.7), C_{44}=12.0(±0.3), $C_{66}=(C_{11}-C_{12})/2$=35.0(±1.1). The numbers in the brackets are 1σ standard deviations and take the uncertainties in the fitting process and (estimated) density errors of 1% into account (Table 1).

It is well-known that the elastic constants recovered from velocity data by inversion of Christoffel's equation can be affected by significant trade-offs [19,20]. To quantitatively evaluate trade–off effects we have calculated correlations between pairs of retrieved constants by normalizing the covariance matrix. We observe marginal correlations between C_{11} and C_{12}, between C_{12} and C_{44}, and between C_{14} and C_{12}. Only the two constants C_{14} and C_{44} are strongly correlated. If we vary these two constants within the range of their reciprocal 1σ uncertainties (cf. Table 1), by keeping constant the combination $C_{44}-0.3C_{14}$, the best fit velocities models are indistinguishable at the 85% confidence level. This is the effect of the particular set of directions probed in our measurements, which do not give independent constraints on C_{12}, C_{14} or C_{44} [17].

The calculated aggregate moduli are: K_{0S}^{V}=37.3(±0.4) GPa and G_0^{V}=24.4(±0.3) GPa for Voigt bounds and K_{0S}^{R}=26.0(±0.3) GPa and G_0^{R}=17.5(±0.4) GPa for Reuss bounds. The Voigt bounds for the average Young's modulus and Poisson's ratio calculated for an isotropic polycrystalline aggregate are E^{V}=60.0(±0.8)) GPa and ν^{V}=0.23(±0.01), while the Reuss bounds are E^{R}=42.8(±1.0)) GPa and ν^{R}=0.23(±0.01). We have also calculated the tighter Hashin–Shtrikman lower and upper bounds [21,22] which are K_{0S}^{HS-}=29.3(±0.4)) GPa, G_0^{HS-}=19.7(±0.4)) GPa, E^{HS-}=48.4(±0.9)) GPa, ν^{HS-}=0.22(±0.01), and K_{0S}^{HS+}=32.5(±0.4)) GPa, G_0^{HS+}=21.8(±0.4)) GPa, E^{HS+}=53.4(±1.0)) GPa, ν^{HS+}=0.23(±0.01),

Table 2
Adiabatic aggregate elastic constants and acoustic velocities of portlandite and brucite; elastic constants are expressed in GPa, velocities are expressed in km/s

	This work (Brillouin)	Laugesen [10] (DFT)*	Holuj et al. [11] (Brillouin)	Mg(OH)2 (Jiang et al., [24]) (Brillouin)
K_{0S}^{V}	**37.3(±0.4)**	36.46	46.9	51.2(±1.0)
K_{0S}^{R}	**26.0(±0.3)**	26.63	32.4	36.4(±0.9)
K_{0S}^{VRH}	**31.6(±0.3)**			43.8(±0.8)
G_0^{V}	**24.4(±0.3)**	22.7	19.3	39.1(±0.5)
G_0^{R}	**17.5(±0.4)**	13.9	13.4	31.3(±0.2)
G_0^{VRH}	**20.9(±0.3)**	18.3	16.3	35.2(±0.3)
K_{0S}^{HS+}	**32.5(±0.4)**			
K_{0S}^{HS-}	**29.3(±0.4)**			
G_0^{HS+}	**21.8(±0.4)**			
G_0^{HS-}	**19.7(±0.4)**			
v_P^{VRH}	**5.15(±0.02)**			6.35(±0.03)
v_S^{VRH}	**3.05(±0.02)**			4.05(±0.03)

V and R denote Voigt and Reuss bounds (VRH Voigt–Reuss–Hill average), HS+ and HS− the upper and lower Hashin–Shtrikmann bounds.
* Density functional theory calculations.
$v_P^{VRH}=[(K_{0S}^{VRH}+4/3G_0^{VHR})/\rho]^{0.5}$; $v_S^{VRH}=(G_0/\rho)^{0.5}$, where ρ=2.242(±0.003)×10^3 (kg/m^3) for portlandite, ρ=2.379(±0.004)×10^3 (kg/m^3) for brucite [24].

Table 3
Aggregate Young's modulus, expressed in GPa, and Poisson's ratio of portlandite

Young's modulus	Poisson's ratio
E^{V}=60.0(±0.8)	ν^{V}=0.23(±0.01)
E^{R}=42.8(±1.0)	ν^{R}=0.23(±0.01)
E^{VRH}=51.4(±1.0)	ν^{VRH}=0.23(±0.02)
E^{HS+}=53.4(±1.0)	ν^{HS+}=0.23(±0.01)
E^{HS-}=48.4(±0.9)	ν^{HS-}=0.22(±0.01)

respectively. The elastic constants are reported in Table 1, the aggregate bulk and shear moduli and corresponding aggregate acoustic velocities in Table 2, and the aggregate Young's modulus and Poisson's ratio in Table 3.

5. Discussion

To our knowledge, there are two data sets of the single crystal elastic constants C_{ij}. Holuj et al. [11] determined the elastic constants by means of Brillouin experiments; Laugesen [10] calculated them by density functional theory. The results of the two studies show large discrepancies for the off-diagonal constants C_{12} (18% difference), and C_{13} (303% difference), and for the shear constant C_{44} (25% difference).

Comparing our new results with those of the two existing studies we observe that the values for the compressional constants C_{11} and C_{33} agree between all the three studies within reciprocal uncertainties. Our result for C_{12} is in agreement with the value calculated by [10], whereas C_{12} determined by [11] differs by 13% from our result. A very large discrepancy exists between the experimental value of C_{13} of [11] and this work—namely 253%. The calculated value C_{13} by [10] is more similar to our result (17% difference) yet incompatible within reciprocal uncertainties. The discrepancy between our results and those of [11] is due to the very limited number of directions sampled in that study, which could not give a good constraint, especially to the value of C_{13}. The shear constant C_{44} determined by [11] agrees with our result within reciprocal uncertainties, whereas the value of C_{44} calculated by [10] is 52% smaller than ours. Finally, [11] reported an upper bound for C_{14} approximately to be 6 GPa, comparable with our result of C_{14}=4.5(±0.2) GPa (a 20% difference). However, due to the relatively weak constraints on the value of this constant Holuj and coworkers [11] assumed C_{14}=0 GPa in their discussion. Also Laugesen [10] in his ab initio study reports C_{14}~0. Our best fit elastic constants are reported in Table 1 together with the results by [10] and [11].

Portlandite exhibits a large elastic anisotropy, both in terms of compressional and shear elastic constants with C_{11}/C_{33}=3.03(±0.09) and C_{66}/C_{44}=2.92(±0.12), which correspond to larger stiffness and rigidity along the more compact basal plane with respect to the axial direction (parallel to the *c*-crystallographic axis) characterized by weak dispersion-type interactions (e.g. [23]). Because of the very large elastic anisotropy, the isotropic aggregate elastic moduli (Table 2) calculated from the single-crystal constants can only give rough bounds to the actual properties of real polycrystalline aggregates, which would be extremely sensitive to the detailed texture. In fact, the ratio between the linear compressibility along the *c*- axis and that along the *a*- axis is equal to 4.65(±0.01) and the ratio between the Young's modulus calculated along the *c*- axis and that along the *a*- axis $E_{[100]}/E_{[001]}$ is equal to 2.7(+/−0.1). The Poisson's ratio of portlandite is also highly anisotropic with ν_{12}=0.32(±0.02), ν31=0.06(±0.01), and ν13=0.17(±0.01), where *i* is the direction of the applied uniaxial stress and *j* is a direction perpendicular to *i*; 1, and 3 are the *a*- and *c*- crystallographic axes and 2 is the direction perpendicular to *a*- on the basal plane.

The difference between the zero pressure Voigt and Reuss bounds to the *adiabatic* bulk modulus of portlandite is 43%, while that between the bounds to the shear is 40%. The tighter Hashin–Shtrikman bounds for both the bulk and the shear modulus differ by 10%. This is typical of highly anisotropic materials like brucite or

Table 4
Grüneisen parameter of portlandite

$\gamma^{V}=1.08(\pm0.02)$
$\gamma^{R}=0.75(\pm0.01)$
$\gamma^{HS+}=0.94(\pm0.02)$
$\gamma^{HS-}=0.85(\pm0.01)$

The Grüneisen parameter γ of portlandite was calculated utilizing the relation $\gamma=\alpha K_{0S}/(\rho C_P)$, (see text). $C_P=1.181\pm0.05$(KJ/(Kg K) [40]; $\alpha=7.65\cdot10^{-5}$ (K^{-1}) [28].
The superscripts V and R denote Voigt and Reuss bounds, HS+ and HS− the upper and lower Hashin–Shtrikman bounds of the bulk moduli K_{0S} used for the calculation.

graphite [24,25]. The aggregate moduli based on our results compare well with the computational results by [10] except for the value of the Reuss bound to the shear modulus, due to the very different value of the shear constant C_{44}. The comparison between our results and those by [11] is less satisfactory, due to the very large difference between the values of both C_{13} and C_{44} which affect both the bulk and shear moduli [6].

In order to convert the isentropic bulk modulus K_{0S} determined by Brillouin spectroscopy into the isothermal bulk modulus K_{0T}, more useful for thermodynamic calculations we need to calculate the thermodynamic Grüneisen parameter γ (e.g. [26] defined as $V(\partial P/\partial U)_V$, where U is the internal energy function. We have calculated the thermodynamic Grüneisen parameter γ of portlandite utilizing the relation $\gamma=\alpha\cdot K_{0S}/(\rho\cdot C_P)$, with α thermal expansion, K_{0S} adiabatic bulk modulus, ρ density and C_P specific heat at constant pressure (Table 4). The difference between γ calculated from the Voigt ($\gamma^{V}=1.08(\pm0.02)$) and Reuss ($\gamma^{R}=0.75(\pm0.01)$) bounds of K_{0S} is about 25%, while that one derived from the Hashin–Shtrikman bounds ($\gamma^{HS+}=0.94(\pm0.02)$; $\gamma^{HS-}=0.85(\pm0.01)$) is less than 10% (Table 4). The Grüneisen parameter for the isostructural brucite $Mg(OH)_2$ is reported to be 0.58 [24], which is significantly lower than the values of the present paper.

The isothermal bulk modulus K_{0T} has been determined, by using the thermodynamic relation $K_{0T}=K_{0S}/(1+\alpha\gamma T)$, where K_{0S} is the isentropic bulk modulus, α the thermal expansion and γ the thermodynamic Grüneisen parameter (Table 5). The Voigt and Reuss bound for the isothermal bulk modulus of Portlandite obtained in this study are 36.4(±0.4) GPa and 25.6(±0.3) GPa, respectively. The low- and high- Hashin–Shtrikman bounds [21] are 28.7(±0.4) GPa and 31.8 (±0.4) GPa. The experimentally determined K_{0T} from high pressure X-ray or neutron diffraction experiments [12,13,27,28] compare well with the range defined by our Brillouin scattering experiments. All the static compression results but [1] constrain the value of K_{0T} closer to the Voigt bound than to the Reuss bound. The bulk modulus determined by [1] is equivalent, within mutual uncertainties with the Voigt bound as determined in our study. The results from [27] and [28] are compatible with the Hashin–Shtrikman bounds within reciprocal uncertainties, while those obtained by [12] and [13] exceed the higher bound (Table 5). This behavior is determined by the effect of nonhydrostaticity in high pressure apparatus and by the large elastic anisotropy of portlandite (e.g. [29] and references herein).

Table 5
Aggregate isothermal bulk modulus of portlandite, all units in GPa

	This work (Brillouin)	M&J	*N*	*P*	*F*	*X*
K_{0T}^{V}	36.4(±0.4)					
K_{0T}^{R}	25.6(±0.3)					
K_{0T}^{HS+}	31.8(±0.4)					
K_{0T}^{HS-}	28.7(±0.4)					
K_{0T}		37.8(±1.8)	34.2(±1.4)	33.1	31.2(±2.3)	32.2(±1.0)

The superscripts V, R, HS+, and HS− denote the Voigt-, Reuss- and the upper and lower Hashin–Shtrikman bounds.
M&J: [1], X-ray diffraction; *N*: [12], X-ray diffraction; *P*: [13], neutron diffraction; *F*: [27], X-ray diffraction; *X*: [28], neutron diffraction.

Table 6
Comparison of the isothermal bulk moduli of oxides and hydroxides

Formula	K_{0T} (GPa)	Formula	K_{0T} (GPa)	Me IR* (Å)
MgO	160 (±2)[a]	$Mg(OH)_2$	43 (±5)[h]	0.720
CaO	111 (±3)[b]	$Ca(OH)_2$	32 (±3)[i]	1.000
MnO	149 (±9)[c]	$Mn(OH)_2$	41 (±3)[j]	0.820
CoO	182 (±3)[d]	$Co(OH)_2$	48 (±1)[k], 73.3(±9.5)[l]	0.735
NiO	196 (±14)[e]	$Ni(OH)_2$	51.8[m], 88 (±7)[n]	0.700
CdO	141 (±18)[f]	$Cd(OH)_2$	37.6 (±2.2)[o]	0.950
FeO**	176 (±4)[g]			0.770

*Effective ionic radii assuming that the ionic radius of six-fold coordinated O^{2-} $r(^{VI}O^{2-})$ is equal to 1.40 Å [32].
**Values inferred for stoichiometric FeO.
[a][41] and references therein. [b][31] and references therein. [c][42–47]. [d][45,48–50]. [e][51–55]. [f][42,47,56]. [g][45,57,58]. [h][24,59–64]. [i][12,13,27], this study. [j][65]. [k][65,66]. [l][33]. [m][67]. [n][34]. [o][68].

The characteristics of the elastic anisotropy of portlandite are largely controlled by the crystal structure of this simple hydroxide. The most important structural unit in all the members of the isostructural brucite ($Mg(OH)_2$) family is represented by basal layers of MeO_6 octahedra (where Me is the divalent metal) in a distorted close packed arrangement. These layers are stacked along the *c*-crystallographic axis and linked by weak interactions mediated by OH^- groups aligned along the *c*-axis at the interlayer. Directions along the basal planes have both larger compressional ($C_{11}\gg C_{33}$) and shear constants ($C_{66}\gg C_{44}$) than the axial direction, making all the members of the brucite family extremely elastically anisotropic [24]. In fact, we observe that the elastic constants of portlandite present the same pattern as those of brucite [24] scaled down, due to the fact that the Ca-O bonds are weaker than the Mg–O bonds. This behavior is similar to that observed in the case of MgO and CaO that are isostructural NaCl-type oxides (e.g. [30,31]).

We notice that comparing the brucite-type hydroxides of Mg, Ca, Mn, Co and Ni with the corresponding NaCl-type oxides the relationship between bulk moduli and ionic radii [32] is preserved but linearly scaled down. This means that the presence of the OH group in isostructural hydroxides just linearly scales the bulk modulus proportionally to the scaling of the MeO_6 structural unit from oxides to hydroxides (Table 6, Fig. 3). Expanding on this apparent systematic behavior, with the exclusion of the anomalous result for $Co(OH)_2$ [33] and $Ni(OH)_2$ [34], we can determine a linear scaling equation $K_{0T}^{hydro}=0.25\ (\pm0.02)\times K_{0T}^{ox}+4$

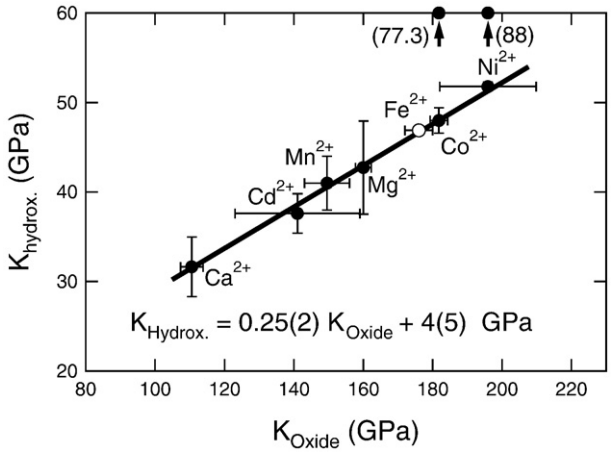

Fig. 3. Systematics of the bulk moduli of NaCl-type oxides and corresponding brucite-type hydroxides. The equation is the least-square fit to the average moduli from the literature, also reported in Table 5. Solid circles: average moduli from the literature (see Table 5). Open circle: FeO–$Fe(OH)_2$ not used in the fit. The labels indicate the metal ion in each oxide-hydroxide couple. The two data points with arrows correspond to the anomalous results for $Co(OH)_2$ and $Ni(OH)_2$ by [32] and [33].

(±5) (where K_{0T}^{hydro} is the isothermal bulk modulus of the hydroxide at ambient conditions, and K_{0T}^{ox} is that of the corresponding oxide). By applying this linear scaling to the average estimated value of the bulk modulus of stoichiometric FeO (K_{0T}=176(±4); see Table 6) we can predict that the bulk modulus of $Fe(OH)_2$—a relevant compound in the early stages of corrosion of steel in reinforced concrete [5,35,36]—is equal to 47 (±6) GPa. The determination of the bulk moduli of the corrosion products formed around the reinforcing bars [37] can lead to improvements in the existing models for the life cycle predictions of corroding reinforced concrete [38].

6. Conclusions

We determined experimentally all the coefficients of the elastic tensor of portlandite by Brillouin scattering. Portlandite exhibits a large elastic anisotropy in compressional and shear elastic coefficients with C_{11}/C_{33}=3.03(±0.09) and C_{66}/C_{44}=2.92(±0.12). This corresponds to a larger stiffness and rigidity in the basal plane with respect the axial direction (parallel to the *c*-axis), the opposite of ettringite, another strongly anisotropic solid component of portland cement [39]. Due to the large elastic anisotropy the Voigt and Reuss bounds to the bulk and shear moduli differ by 43%, and 40%, implying that the moduli of a real aggregate will strongly depend by the textural and mechanical relationship between the mineral grains. Our results for portlandite confirm that the presence of OH groups linearly scales down the bulk modulus according to the size ratios of the MeO_6 structural units from NaCl-type oxides to corresponding brucite-type hydroxides.

Acknowledgments

The GeoForschungsZentrum Potsdam is part of the Helmholtz Gemeinschaft. P.J.M.M. and H.R.W. appreciate support from the KAUST.

References

[1] C. Meade, R. Jeanloz, Static compression of $Ca(OH)_2$ at room temperature: observations of amorphization and equation of state measurements to 10.7 GPa, Geophys. Res. Lett. 17 (1990) 1157–1160.
[2] L. Desgranges, G. Calvarin, G. Chevrier, interactions in M(OH)2: a neutron difffraction study of $Mg(OH)_2$, Acta Cryst., B 52 (1996) 82–86.
[3] L. Desgranges, D. Grebille, G. Calvarin, G. Chevrier, N. Floquet, J.C. Niepce, Hydrogen thermal motion in calcium hydroxide Ca(OH)2, Acta Cryst., B 49 (1993) 812–817.
[4] J.D. Birchall, A.J. Howard, J.A. Bailey, On the hydration of Portland cement, Proc. R. Soc. Lond., A 360 (1978) 445–463.
[5] P.K. Mehta, P.J.M. Monteiro, Concrete: Microstructure, Properties, and Materials, McGraw-Hill, New York, 2006.
[6] R.J. Detwiler, P.J.M. Monteiro, H.R. Wenk, Z. Zhang, Texture of calcium hydroxide near the cement paste-aggregate interface, Cem. Concr. Res. 18 (1988) 823–829.
[7] P.J.M. Monteiro, O.E. Gjorv, P.K. Mehta, Microstructure of the steel-cement paste interface in the presence of chloride, Cem. Concr. Res. 15 (1985) 781–784.
[8] I.P. Swainson, E.M. Schulson, A neutron diffraction study of ice and water within a hardened cement paste during freeze–thaw, Cem. Concr. Res. 31 (2001) 1821–1830.
[9] E.M. Schulson, I.P. Swainson, T.M. Holden, Internal stress within hardened cement paste induced through thermal mismatch. Calcium hydroxide versus calcium silicate hydrate, Cem. Concr. Res. 31 (2001) 1785–1791.
[10] J.L. Laugesen, Density functional calculations of elastic properties of portlandite, $Ca(OH)_2$, Cem. Concr. Res. 35 (2005) 199–202.
[11] F. Holuj, M. Drozdowski, M. Czajkowski, Brillouin spectrum of $Ca(OH)_2$, Solid state Commun. 56 (1985) 1019–1021.
[12] T. Nagai, T. Ito, T. Hattori, T. Yamanka, Compression mechanism and amorphization of portlandite, $Ca(OH)_2$: structural refinement under pressure, Phys. Chem. Min. 27 (2000) 462–466.
[13] A. Pavese, M. Catti, G. Ferraris, S. Hull, P–V equation of state of portlandite, $Ca(OH)_2$, from powder neutron diffraction, Phys. Chem. Min. 24 (1997) 85–89.
[14] J.R. Sandercock, Trends in Brillouin scattering: studies of opaque materials, supported films, and central modes, in: M. Cardona, G. Guntherodt (Eds.), Light Scattering in Solids III: Recent Results, Topics in Appl.Physics. Eds. Springer Verlag, Berlin, 1982.
[15] C.H. Whitfield, E.M. Brody, W.A. Bassett, Elastic moduli of NaCl by Brillouin scattering at high pressure in a diamond anvil cell, Rev. Sci. Instrum. 47 (1976) 942–947.
[16] C.-C. Chen, C.-C. Lin, L.G. Liu, S.V. Sinogeikin, J.D. Bass, Elasticity of single-crystal calcite and rhodochrosite by Brillouin spectroscopy, Am.Min. 86 (2001) 1525–1529.
[17] B. Auld, Acoustic Fields and Waves in Solids, John Wiley, Hoboken, N.Y., 1973.
[18] R.E. Newnham, Properties of materials, Oxford University Press, Oxford, 2005.
[19] C.-S. Zha, T.S. Duffy, R.T. Downs, H.-K. Mao, R.J. Hemley, Sound velocity and elasticity of single-crystal forsterite to 16 GPa, J. Geophys. Res., B 101 (1996) 17535–17545.
[20] Z. Mao, S.D. Jacobsen, F. Jiang, J.R. Smyth, C.M. Holl, D.J. Frost, T.S. Duffy, crystal elasticity of wadsleyites, β-Mg_2SiO_4, containing 0.37–1.66 wt.% H_2O, Earth Planet. Sci. Lett. 266 (2008) 78–89.
[21] Z. Hashin, S. Shtrikman, On variational approach to the theory of the elastic behaviour of polycrystals, J. Mech. Phys. Solids 10 (1962) 335–342.
[22] J.P. Watt, L. Peselnik, Clarification of the Hashin–Shtrikman bounds on the effective elastic moduli of polycrystals with hexagonal, trigonal, and tetragonal symmetries, J. Appl. Phys. 51 (1980) 1525–1531.
[23] P. Baranek, A. Lichanot, R. Orlando, R. Dovesi, Structural and vibrational properties of solid $Mg(OH)_2$ and $Ca(OH)_2$—performances of various Hamiltonians, Chem. Phys. Let. 340 (2001) 362–369.
[24] F. Jiang, S. Speziale, T.S. Duffy, Single-crystal elasticity of brucite, $Mg(OH)_2$ to 15 GPa by Brillouin scattering, Am. Min 91 (2006) 1893–1900.
[25] O.L. Blakslee, D.G. Proctor, E.J. Seldin, G.B. Spence, T. Weng, Elastic constants of compression-annealed pyrolitic graphite, J. Appl. Phys. 46 (1970) 3373–3382.
[26] J.-P. Poirier, Introduction to the Physics of the Earth's Interior, Canbridge University Press, Cambridge, 2000.
[27] H. Fukui, O. Ohtaka, T. Fujisawa, T. Kunisada, T. Suzuki, T. Kikegawa, Thermo-elastic properties of $Ca(OH)_2$ portlandite, High Press. Res. 23 (2003) 55–61.
[28] H. Xu, Y. Zhao, J. Zhang, D.D. Hickmott, L.L. Daemen, In situ neutron diffraction study of deuterated portlandite $Ca(OD)_2$ at high pressure and temperature, Phys. Chem. Min. 34 (2007) 223–232.
[29] R.A. Angel, M. Bujak, J. Zhao, G.D. Gatta, S.D. Jacobsen, Effective hydrostatic limits of pressure media for high-pressure crystallographic studies, Appl. Crystall. 40 (2007) 26–32.
[30] S.V. Sinogeikin, J.D. Bass, Single-crystal elasticity of pyrope and MgO to 20 GPa by Brillouin scatterimng in the diamond anvil cell, Phys. Earth Planet. Inter. 120 (2000) 43–62.
[31] S. Speziale, S.R. Shieh, T.S. Duffy, High-pressure elasticity of calcium oxide: a comparison between Brillouin spectroscopy and radial X-ray diffraction, J. Geophys.Res. 111 (2006) B02203, doi:10.1029/2005JB003823.
[32] R.D. Shannon, C.T. Prewitt, Coordination and volume changes accompanying high-pressure phase transformations of oxides, Mat. Res. Bull. 4 (1969) 57–62.
[33] J.H. Nguyen, M.B. Kruger, R. Jeanloz, Evidence for "partial" (sublattice) amorphization in $Co(OH)_2$, Phys. Rev. Lett. 78 (1997) 1936–1939.
[34] N. Garg, S. Karmakar, S.M. Sharma, E. Busseto, S.K. Sikka, High-pressure X-ray diffraction studies on β-$Ni(OH)_2$, Physica B 349 (2004) 245–250.
[35] S. Joiret, M. Keddam, X.R. Nóvoa, M.C. Perez, C. Rangel, T. Takenouth, Use of EIS, ring-disk electrode, EQCM and Raman spectroscopy to study the film of oxides formed on iron in 1 M NaOH, Cem. Concr. Compos. 24 (2002) 7–15.
[36] M.S. Odziemkowski, T.T. Schuhmaker, R.W. Gillham, E.J. Reardon, Mechanism of oxide transformation on iron in simulating groundwater solutions: Raman spectroscopic studies, Corros. Sci. 40 (1998) 371–389.
[37] P.J.M. Monteiro, O.E. Gjorv, P.K. Mehta, Microstructure of the steel-cement paste interface in the presence of chloride, Cem. Concr. Res. 15 (1985) 781–784.
[38] R. Piltner, P.J.M. Monteiro, Stress analysis of expansive reactions in concrete,, Cem. Concr. Res. 30 (2000) 843–848.
[39] S. Speziale, F. Jiang, Z. Mao, P.J.M. Monteiro, H.R. Wenk, T.S. Duffy, F.R. Schilling, Single-crystal elastic constants of natural ettringite, Cem. Concr. Res. 38 (2008) 885–889.
[40] W.E. Hatton, D.L. Hildebrand, G.C. Sinke, The chemical thermodynamic properties of calcium hydroxide, Am. Chem. Soc. J. 81 (1959) 5028–5030.
[41] S. Speziale, C.-S. Zha, T.S. Duffy, H.-K. Mao, R.J. Hemley, Quasi-hydrostatic compression of magnesium oxide to 52 GPa: implications for the pressure–volume–temperature equation of state, J. Geophys. Res. 106 (2001) 515–528.
[42] H.G. Drickamer, R.W. Linch, R.L. Clendenen, E.A. Perez-Albuerne, X-ray diffraction studies of the lattice parameters of solids under very high pressure, Solid state Phy. 19 (1966) 135–229.
[43] R. Jeanloz, A. Rudy, Static compression of MnO manganosite to 60 GPa, J. Geophys. Res. 92 (1987) 11433–11436.
[44] R.E. Pacalo, E.K. Graham, Pressure and temperature dependence of the elastic properties of synthetic MnO, Phys. Chem. Min. 18 (1991) 69–80.
[45] Y. Sumino, M. Kumazawa, O. Nishizawa, W. Pluschkell, The elastic constants of single crystal $Fe_{1-x}O$, MnO and CoO, and the elasticity of stoichiometric magnesiowüstite, J. Phys. Earth 28 (1980) 475–495.
[46] S.L. Webb, J. Fitz Gerald, High-pressure elasticity, shear mode softening and polymorphism in MnO, Phys. Earth Planet. Inter. 52 (1988) 117–131.
[47] J. Zhang, Room-temperature compressibilities of MnO and CdO: further examination of the role of cation type in bulk modulus systematics, Phys. Chem. Min. 26 (1999) 644–648.
[48] K.S. Aleksandrov, L.A. Shabanova, L.M. Reshchikova, Anomalies of elastic properties and internal friction of a CoO single crystal, Sov. Phys. Solid State 10 (1968) 1316–1321.
[49] Q. Guo, H.-K. Mao, J. Shu, R.J. Hemley, The phase transitions of CoO under static pressure to 104 GPa, J. Phys., Condens. Matter 14 (2002) 11369–11374.
[50] N. Uchida, S. Saito, Elastic constants and acoustic absorption coefficients in MnO, CoO, and NiO single crystals at room temperature, J. Acoust. Soc. Am. 51 (1972) 1602–1605.
[51] R.L. Clendenen, H.G. Drickamer, Lattice parameters of nine oxides and sulfides as a function of pressure, J. Chem. Phys. 44 (1966) 4223–4228.
[52] E. Huang, Compression behavior of NiO in a diamond cell, High Press. Res. 13 (1995) 307–319.

[53] I. Wakabayashi, H. Kobayashi, H. Nagasaki, S. Minomura, The effect of pressure on the lattice parameters Part II. Gd, NiO, and β-MnS, J. Phys. Soc. J. 25 (1968) 227–233.
[54] M.H. Manghani, L.J. Wang, S. Usha-Devi, L.C. Ming, Isothermal compression measurements on Fe, SiO_2, NiO to 24 GPa at room temperature, EOS 73 (1992) 579.
[55] Y. Noguchi, M. Uchino, H. Hikosaka, T. Atou, K. Kusaba, K. Fukuoka, T. Mshimo, Y. Syono, Equation of state of NiO studied by shock compression, J. Phys. Chem. Solids 60 (1999) 509–514.
[56] H. Liu, H.K. Mao, M. Somayazulu, Y. Ding, Y. Meng, D. Häusermann, B1- to B2-phase transition of transition-metal monoxide CdO under strong compression, Phys. Rev. B 70 (2004) 94114, doi:10.1103/PhysRevB.70.094114.
[57] R. Jeanloz, Y. Sato-Sorensen, Hydrostatic compression of $Fe_{(1-x)}O$ wuestite, J. Geophys. Res. 91 (1986) 4665–4672.
[58] J. Zhang, Effect of defects on the elastic properties of wüstite, Phys. Rev. Lett. 84 (2000) 507–509.
[59] M. Catti, G. Ferraris, S. Hull, A. Hull, Static compression and H disorder in Mg(OH)2 to 11 GPa: a powder diffraction study, Phys.Chem. Min. 22 (1995) 200–206.
[60] T.S. Duffy, T.J. Ahrens, M.A. Lange, The shock-wave equation of state of brucite Mg $(OH)_2$, J. Geophys.Res. 96 (1991) 14319–14330.
[61] T.S. Duffy, J. Shu, H.K. Mao, R.J. Hemley, Single-crystal X-ray diffraction of brucite to 14 GPa, Phys.Chem. Min. 22 (1995) 277–281.
[62] J.B. Parise, K. Leinenweber, D.J. Weidner, K. Tan, R.B. Von Dreele, Pressure-induced H bonding: neutron diffraction study of brucite $Mg(OD)_2$, to 9.3 GPa, Am.Min. 79 (1994) 193–196.
[63] X. Xia, D.J. Weidner, Y. Zhao, Equation of state of brucite: single-crystal Brillouin spectroscopy study and polycrystalline pressure–volume–temperature measurements, Am. Min. 83 (1998) 68–74.
[64] H. Fukui, O. Ohtaka, T. Suzuki, F. Funakoshi, Thermal expansion of $Mg(OH)_2$ brucite under high pressure, and pressure dependence of entropy, Phys.Chem. Min. 30 (2003) 511–516.
[65] J.B. Parise, B. Theroux, R. Li, J.S. Loveday, W.G. Marshall, S. Klotz, Pressure dependence of hydrogen bonding in metal deuteroxides: a neutron powder diffraction study of Mn(OD)2 and β-Co(OD)2, Phys. Chem. Min. 25 (1998) 130–137.
[66] S.R. Shieh, T.S. Duffy, Raman spectroscopy of $Co(OH)_2$ at high pressures: implications for amorphization and hydrogen repulsion, Phys.Rev., B 66 (2002) 134301, doi:10.1103/PhysRevB.66.134301.
[67] J.B. Parise, H. Cox, H. Kagi, R. Li, W. Marshall, J. Loveday, S. Klotz, Hydrogen bonding in $M(OD)_2$ compounds under pressure, Rev. High Press. Sci. Technol. 7 (1998) 211–216.
[68] S.-H. Shim, S. Rekhi, M.C. Martin, R. Jeanloz, Vibrational spectroscopy and X-ray diffraction of $Cd(OH)_2$ to 28 GPa at 300 K, Phys. Rev., B 74 (2006) 024107-024101–024107-024110.